# Accepted Version

# Turbulence characteristics in the wake of a heliostat in an atmospheric boundary layer flow

Azadeh Jafari[1, *], Matthew Emes[1], Benjamin Cazzolato[1], Farzin Ghanadi[2], Maziar Arjomandi[1]

[1] *Centre for Energy Technology, School of Mechanical Engineering, University of Adelaide, Adelaide, SA 5005, Australia.*

[2] *School of Engineering, University of Newcastle, Callaghan, NSW 2308, Australia.*

*Corresponding author: azadeh.jafari@adelaide.edu.au

## Abstract

The mean and spectral characteristics of turbulence in the wake flow of a flat plate model resembling a heliostat in the atmospheric boundary layer flow are investigated in a wind tunnel experiment. Mean velocity and turbulence kinetic energy were characterised in the wake of a heliostat model at three elevation angles up to a distance of eight times the characteristic dimension of the heliostat panel. An increase in turbulence intensity and kinetic energy was found in the wake flow, reaching a peak at a distance equal to approximately twice the characteristic dimension of the heliostat panel. Furthermore, spectral and wavelet analysis of velocity fluctuations in the wake showed that the dominant mechanism in the immediate downstream of the plate was breakdown of large inflow turbulence structures to smaller scales. In the end, the wake-induced turbulence patterns and wind loads in a heliostat field were discussed. It was found that compared to a heliostat at the front row, the heliostats positioned in high-density regions of a field were subjected to a higher turbulence intensity, and consequently larger dynamic wind loading. The results show that it is necessary to consider the increased unsteady wind loads for the design of heliostat in high-density regions of a field, where the gap between the rows is less than three-times the characteristic length of the heliostat panel.

# 1   Introduction

Understanding the flow characteristics in the wake of a heliostat is a fundamental step for analysis of the flow turbulence within a heliostat field which has several complexities including its dependence on the field arrangement and density. This knowledge accompanied with measurements of in-field wind loads on full-scale structures can be used to predict the wind loads in a heliostat field, which is important for the field design. As an example, heliostats placed in regions of increased turbulence intensity need to be designed to withstand larger unsteady and dynamic forces requiring higher mechanical impedance of the support structure. Furthermore, by determination of the regions of the field where the mean and unsteady wind loads are lower, the structural stiffness and foundation depth can be decreased. As the heliostat field constitutes between 40% to 50% of the total capital cost of a solar plant (Kolb, 2011), modification of the design of heliostats can help to reduce the capital cost. This study focuses on the wake of a heliostat in an atmospheric boundary layer and aims to develop an understanding of how the statistical and spectral characteristics of turbulence change in the wake of the heliostat. The findings are however not limited to heliostats and provide an insight into the turbulence in the wake of other flat-plate-like structures in the atmospheric boundary layer including solar photovoltaic panels, billboards and wind barriers.

Heliostats in a solar field are arranged in rows surrounding a receiver in a central or a polar design, with a gap between the subsequent rows which typically varies from a value equal to the characteristic length of the mirror panel to about 8-times the characteristic length as the heliostats are installed further away from the central tower (Hui, 2011). Heliostats within the field are exposed to the turbulence in the wake of other heliostats or the solar tower which alters the approaching turbulence in the atmospheric boundary layer. Based on the field arrangement and the gap between the heliostat rows, both the mean flow and turbulence characteristics inside the field can be very different from the incoming conditions. For instance, wind velocity measurements by ultrasonic anemometers in a five-row array of heliostats in a field found an increase in turbulence intensity from 10% in the approaching flow to 50% in the second row of heliostats (Sment and Ho, 2014). Available field measurements are however very limited due to the complexity of field measurements and the variations of velocity and intensity and length scales of turbulence in a heliostat field are not well known. The increased turbulence in the field is related to the vortex shedding in the wake of heliostats. A large eddy simulation of the flow field around a heliostat, at an elevation angle $\alpha = 25°$, in a uniform inflow showed formation of coherent turbulence structures and counter rotating vortices in the

wake (Boddupalli *et al.*, 2018), which subject the downstream structures to dynamic loading. Experimental investigations of the wind loads on multiple heliostats also show the changes in the wind loads from a single heliostat. For instance, measurements of surface pressure distribution on a second heliostat placed in tandem of another one in an atmospheric boundary layer flow showed significant changes in the pressure distribution on the second heliostat, which varied with the gap between the two heliostats (Jafari *et al.*, 2019c). Furthermore, Peterka *et al.* (1987b) measured the wind loads in a four-row arrangement of heliostat models in a wind tunnel experiment and found that while the mean drag force coefficient on a heliostat in the fourth row was lower than that for a heliostat in the first row, the peak drag force coefficient was larger. The increase in the peak drag force suggests an increase in the turbulence intensity in the wake of the upstream heliostats. Hence, understanding how the flow turbulence changes inside the field can help to provide an estimate of the changes in the unsteady wind loads on in-field heliostats.

The flow past a heliostat, if excluding the support structure and the pylon, is similar to the flow past a flat plate at different angles of attack. The wake of a flat plate in a uniform flow, which is a widely studied subject, is characterised by flow separation and vortex shedding. The blockage of the flow by the bluff body creates a velocity deficit in the wake accompanied with periodic velocity fluctuations due to vortex shedding. Three-dimensional and large coherent turbulence structures are formed in the wake. Turbulence intensity in the wake of a square flat plate normal to a uniform flow can increase by up to 16% in the near wake (Nedić *et al.*, 2013). The angle of attack, which resembles the elevation angle of a heliostat panel during its operation, affects the symmetry of the wake. While the wake of a flat plate normal to a uniform flow is symmetric, when inclined at different angles to the flow, the wake becomes asymmetric due to the unequal strength of vortices shed from the leading and trailing edges, resulting in an asymmetric velocity deficit in the wake (Lam and Leung, 2005; Yang *et al.*, 2012).

Inflow turbulence impacts the wake dynamics including structure of turbulence and vortex shedding. Experimental investigation of the wake of flat disks normal to a grid-generated turbulent flow showed the effect of turbulence length scale and kinetic energy in the incoming flow on the flow around the disk (Humphries and Vincent, 1976). Increase of incoming turbulence enhanced mixing in the shear layer and increased entrainment of fluid into the wake, and consequently, decreased the wake recovery length over which the flow properties returned to the undisturbed condition. A large eddy simulation of the wake behind a sphere developed in a turbulent pipe flow also showed that the incoming turbulence resulted in a wider

radial expansion of the wake and a faster recovery of velocity deficit along the wake centreline (Legendre *et al.*, 2006). Hearst *et al.* (2016) studied the wake of a wall-mounted cube in four turbulent boundary layers with grid-generated turbulence intensities between 5.4% and 9%. At constant inflow shear level, the wake recovered faster for larger inflow turbulence intensities. In contrast, shear at the cube height was found to have a stronger impact on the flow recovery when comparing wakes with different values of inflow velocity gradient. On the other hand, inflow turbulence is found to have a stronger effect than mean shear at large inflow turbulence intensities (Amoura *et al.*, 2010). An experimental investigation of the effect of inflow turbulence on the wake of a sphere, with inflow turbulence intensities between 15% and 26% and length scales of 3–4 times larger than the sphere diameter, showed that turbulence and velocity deficit in the far wake scaled with the intensity of incoming turbulence (Amoura *et al.*, 2010). It was found that existence of the incoming turbulence altered the wake flow characteristics as the wake instabilities were mainly resulted from the distortion of the incident turbulence, and not the mean velocity, by the sphere. Furthermore, an experimental study of the effect of grid-generated turbulence, with turbulence intensities between 0.8% and 4.3%, on the wake of a disk normal to the flow found that the inflow turbulence weakened vortex shedding in the near wake and reduced its strength (Rind and Castro, 2012). The turbulence decay rate in the far wake was significantly varied by the inflow turbulence such that the wake turbulence evolved towards the inflow characteristics eventually. The observed effects were found to be stronger when the freestream turbulence intensity was larger than 3%. These findings suggest that the inflow turbulence significantly influences the dynamics of wake instabilities and turbulence within the wake flow. Heliostats are placed in the lower the 10 m of the turbulent atmospheric boundary layer and are subjected to large velocity gradients and large-scale turbulence structures. Hence, the inflow turbulent boundary layer alters the wake of a heliostat from a flat plate developed in a uniform flow.

Another parameter, in addition to the inflow turbulence, which affects the wake of a heliostat is the ground effect. The mirror panel of a heliostat is hinged on a pylon such that there is typically a gap between the bottom edge of the panel and the ground which varies with the elevation angle of the panel. The studies on bluff body wakes in a uniform flow show that decreasing the gap from the ground beyond a certain threshold can suppress vortex shedding (Bearman and Zdravkovich, 1978; Bosch *et al.*, 1996). Furthermore, investigation of the effect of the gap flow on the wake of a sharp-edged flat plate suspended in a water channel showed formation of a wall jet which influenced the near wake significantly (Krampa-Morlu and

Balachandar, 2007; Shinneeb and Balachandar, 2016a). It was found that when the gap increased, the reverse flow in the wake was eliminated and the streamwise velocity fluctuations were decreased (Shinneeb and Balachandar, 2016b).

The present study aims to develop an understanding of the turbulence characteristics in the wake of a heliostat in an atmospheric boundary layer flow. Extensive velocity measurements were conducted in the wake of a flat plate model representing a heliostat in two simulated neutral atmospheric boundary layer flows in the University of Adelaide large-scale wind tunnel to characterise turbulence in the wake flow. The remainder of this paper is organised as follows. A description of the experimental method is presented in Section 2. In Section 3, the wake flow and turbulence were characterised by statistical and spectral analysis of the velocity measurements. The findings are then used as a basis for prediction of how wind loads in a heliostat field change in Section 4. Finally, conclusions are given in Section 5.

## 2  Methodology

Experimental measurements were performed in the University of Adelaide large-scale wind tunnel. The working section of the boundary layer wind tunnel is 3 m $\times$ 3 m $\times$ 17 m, and the turbulence intensity in the empty tunnel is between 1% and 3%. Spires and floor roughness elements were used to simulate the atmospheric boundary layer in the wind tunnel. Five spires with identical dimensions were placed at the inlet of the test section with a centre-line distance of 0.5 m in the lateral ($y$) direction. The spires were followed by a 7.2 m streamwise fetch of wooden roughness elements covering approximately 24% of the floor area over the fetch length. The sizing and spacing of the roughness elements were similar to previous experiment by the authors (Jafari *et al.*, 2019c). In order to minimise the parameters affecting the wake flow, it was attempted to create two boundary layers of a similar height so that the relative position of the models in the boundary layers, $H/\delta$, does not change. Therefore, the spires for the two boundary layers, boundary layer A and B, were designed with an identical height (1.3 m). Figure 1(a–b) show the test setup at the test section containing spires, roughness elements and the heliostat model. The heliostat model consists of a pylon (height =130 mm and thickness=10 mm), and a square panel with a characteristic length of 200 mm and a thickness of 2 mm. The heliostat model height to panel characteristic length ratio, $H/c$, is 0.65, which according to Pfahl (2018) is conventional for heliostats. Furthermore, the blockage ratio, defined as the ratio of the frontal area of the heliostat model panel to the tunnel cross-sectional area, has a maximum value of 0.44% when the heliostat panel is normal to the flow, which is

insignificant and hence blockage does not affect the measurements as the maximum allowable blockage ratio is 10% (Barlow *et al.*, 1999).
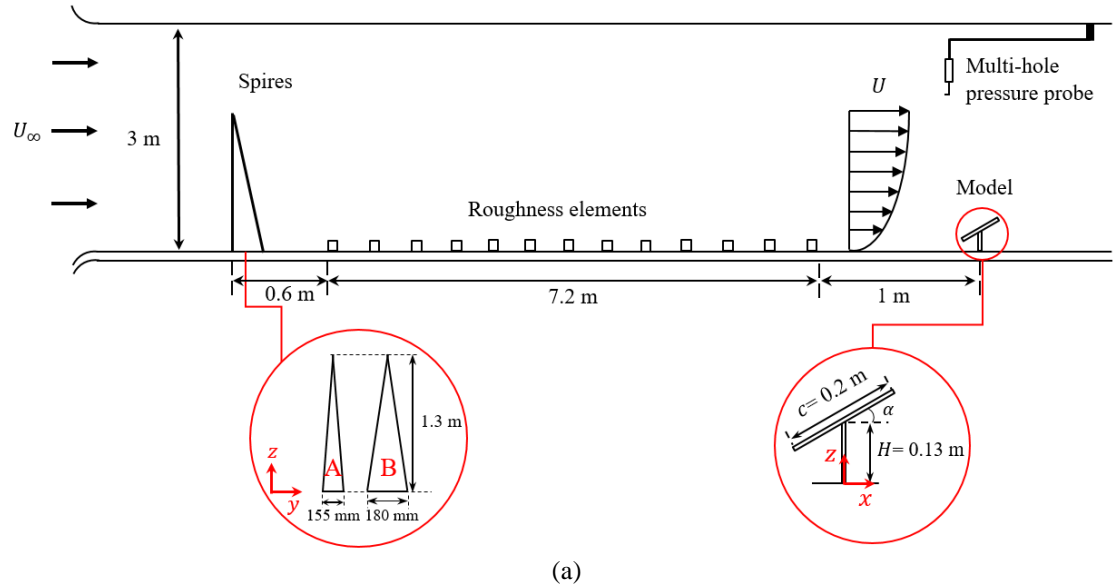


(a)



(b)

Figure 1: The experimental setup in the University of Adelaide wind tunnel. (a) Schematic of the setup, (b) photograph of the setup looking upstream from the plate.

The inflow conditions and the wake behind the heliostat model were measured using a Turbulent Flow Instrumentation (TFI) multi-hole pressure probe (Cobra probe), which is capable of measuring the three unsteady velocity components and the local static pressure. The accuracy of the measured velocity by the multi-hole pressure probe is within $\pm0.5$ m/s and $\pm1°$ in pitch and yaw angles for turbulence intensities of up to 30% according to the manufacturer datasheet. The turbulence intensities in this study are generally below this limit except at immediate near-wake regions. Furthermore, the measurement error of mean velocity calculated

as the standard deviation of five identical measurements was found to be 1.1%. Cobra probes have been found to provide reasonable accuracy for measurement of complex turbulent flows in the literature. Cobra probes have been used in the literature (Vino *et al.*, 2003; Bell *et al.*, 2014; Peng *et al.*, 2016; Gilhome, 2017; Lam and Peng, 2017; Aliferis *et al.*, 2019) for study of both time-averaged and time-resolved velocity and turbulence characteristics in the wake flow. Furthermore, a comparison of the velocity measurements obtained by a Cobra probe with those from laser Doppler anemometry and hot wire anemometry in a turbulent pipe flow and in the wake of a wind turbine showed that the maximum error in the mean velocity and turbulence intensity measured by the Cobra probe were 2% and 1%, respectively (Draskovic, 2017).

### 2.1    Incoming Flow Conditions

The two simulated boundary layers in the wind tunnel were characterised and their mean velocity and turbulence characteristics were determined. Velocity was measured, in the absence of the heliostat model, over an area of 1 m$^2$ in the lateral-wall normal planes at different streamwise locations starting from 1 m downstream of the roughness fetch over a length of 1.6 m ($x/c$=8) to investigate the boundary layer development. The vertical profiles of mean velocity, $U$, normalised with the free-stream velocity, $U_\infty$, streamwise and vertical turbulence intensities, $I_u = \sigma_u/U$ and $I_w = \sigma_w/U$, and normalised Reynolds shear stress, $-uw/U_\infty^2$, for the two boundary layers measured at the location of the model ($x$=0, and $y$=0) and in its absence are given in Figure 2. Figure 2(a) shows the non-dimensional mean velocity profiles of the two boundary layers. The boundary layer thickness ($\delta$) was determined as $\delta_{0.99}$ from the mean velocity profile as 0.98 m and 1.1 m for boundary layer A and B, respectively. The mean velocity profiles of the two boundary layers match logarithmic profiles with aerodynamic surface roughness values of 0.002 m and 0.0026 m, respectively. According to Figure 2(b), the longitudinal turbulence intensity at the model hinge height ($z/c$=0.65) is 13% and 15% in boundary layer A and B, respectively. Furthermore, vertical turbulence intensity at the model hinge height is 8% and 10% in boundary layer A and B, respectively (Figure 2(c)). The normalised Reynolds shear stress profiles in Figure 2(d) show the largest magnitude of the Reynolds shear stress at $z/c$=2 in boundary layer B and an approximately constant shear stress between $z/c$=1 and 3 for boundary layer A. For the analysis of the wake flow characteristics in the current study, only the mean velocity and turbulence characteristics in the simulated wind tunnel boundary layers are presented. A detailed discussion of the similarities and differences of the mean velocity and turbulence intensity profiles, as well as spectral

characteristics and length scales of turbulence in the wind tunnel boundary layers and the atmospheric boundary layer is given in Jafari *et al.* (2019c).
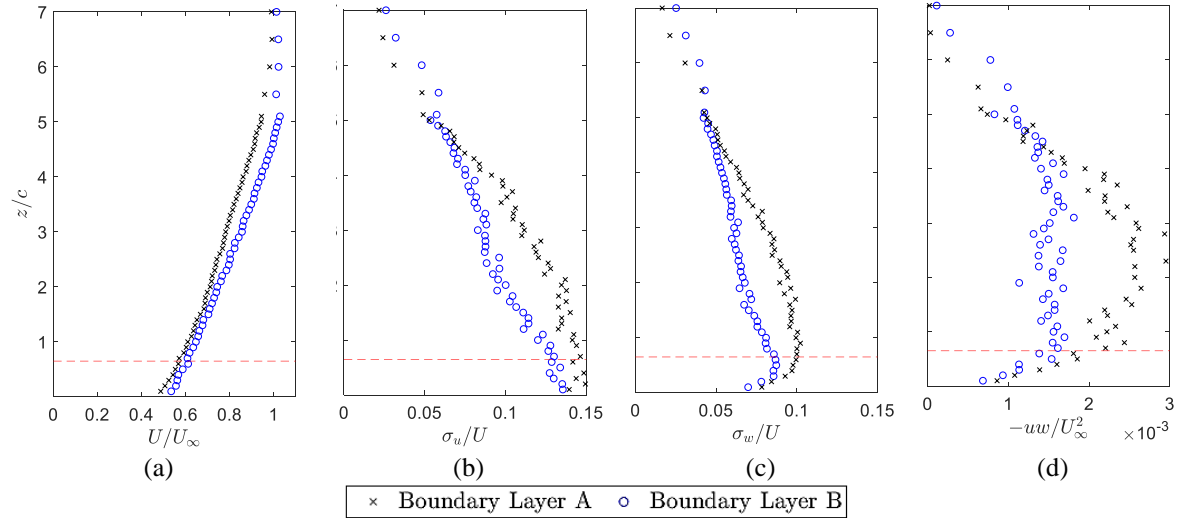


Figure 2: Profiles of the incoming flow in the two wind tunnel boundary layers: (a) normalised mean velocity, (b) longitudinal turbulence intensity, (c) vertical turbulence intensity, and (d) Reynolds shear stress (at $U_\infty$ =11.1 m/s, $x$=0, and $y$=0). The horizontal dashed lines show the model hinge height.

Table 1 gives a summary of the inflow conditions, including boundary layer height and longitudinal and vertical turbulence intensities at the model location for each boundary layer flow. In addition, the ratio of longitudinal and vertical integral length scales ($L_u^x$ and $L_w^x$) to the characteristic dimension of the plate are presented. The turbulence intensities and integral length scale ratios are given at the hinge height of the model, $H$, since this value is constant for all elevation angles, while the height of the plate top edge varies, and hence, $H$ provides a comparison for all cases. The non-dimensional shear $\tau_H = (H/U_H)(\partial U/\partial z)|_H$ is also given in Table 1. This non-dimensional form of shear is selected as recommended by Hearst *et al.* (2016) as free-stream measurements in the atmospheric surface layer are not usually available. Hence, $\tau_H$ is normalised with the time scale of the flow at the hinge height of the model.

Table 1: Incoming flow conditions. The characteristics given at the model position were calculated from velocity measurements in the absence of the model.

|  | $\delta$ | $H/\delta$ | $U_H/U_\infty$ | $\tau_H$ | $I_{u_H}$ | $I_{w_H}$ | $(L_u^x/c)_H$ | $(L_w^x/c)_H$ |
|---|---|---|---|---|---|---|---|---|
| Boundary Layer A | 0.98 | 0.133 | 0.56 | 0.048 | 0.13 | 0.08 | 2.01 | 0.42 |
| Boundary Layer B | 1.20 | 0.108 | 0.61 | 0.028 | 0.15 | 0.10 | 2.40 | 0.48 |

Furthermore, to achieve similarity in the wind tunnel experiments, ideally, both the boundary layer and the heliostat model must be scaled down by an identical length scale factor. However, this similarity cannot be achieved for small-scale structures such as heliostats and solar panels as it requires the model dimensions to be very small. The inevitable consequence of the mismatch of length scale factors is a change in $H/\delta$ and a different $L_u^x/c$ and $L_w^x/c$ between the wind tunnel and the full-scale conditions. This scaling issue has been extensively discussed in the literature (Tieleman, 2003; Richards *et al.*, 2007; Jafari *et al.*, 2019c) and its discussion is out of the scope of the current study. However, with consideration of the differences, the results are interpreted with respect to the inflow conditions for characterisation of the wake flow.

### 2.2 Wake Measurements

The velocity in the wake of the heliostat model at elevation angles of $\alpha$=30°, 60°, and 90° were measured within the two boundary layers. These elevation angles are considered to represent a range of operational angles for heliostats. Velocity measurements were performed over streamwise wall normal planes downstream of the heliostat model at $y$=0 mm. Figure 3 shows the measurement grid which was determined based on initial measurements and evaluation of the resolution of the results. The measurement grid ranges from $z$=10 mm to $z$=500 mm in the vertical direction, with a grid spacing $\Delta z$=20 mm. In the streamwise direction, the measurements were taken at positions ranging from $x$=150 mm to $x$=1600 mm downstream of the model, with $\Delta x$ increasing from 50 mm in the near wake to a maximum of 200 mm at $x$=1000–1600 mm. Velocity measurements were acquired for a duration of 30 seconds at each point with a sampling frequency of 2 kHz. The measurements for spectral analysis were taken over a duration of 120 seconds. A low-pass filter was applied to all the measured velocity signals filtering them at 900 Hz to avoid aliasing. This frequency response is deemed sufficient for the current measurements as the entire energy containing frequencies are resolved. Furthermore, estimation of the spatial resolution of the Cobra probe shows that the velocity measurements are of acceptable accuracy. Based on Taylor's frozen turbulence theory, for a frequency response of 900 Hz, and the maximum mean velocity at measurement locations equal to 6.77 m/s (corresponding to the mean inflow velocity at the heliostat hinge height in Boundary Layer B), the minimum spatial resolution of the probe is approximately 1.19 mm. This minimum resolvable length scale is two orders of magnitude smaller than the plate chord length (200 mm) and the integral length scale of the two inflow boundary layers (402 mm and 480 mm), and three orders of magnitude smaller than the depth of the boundary layer
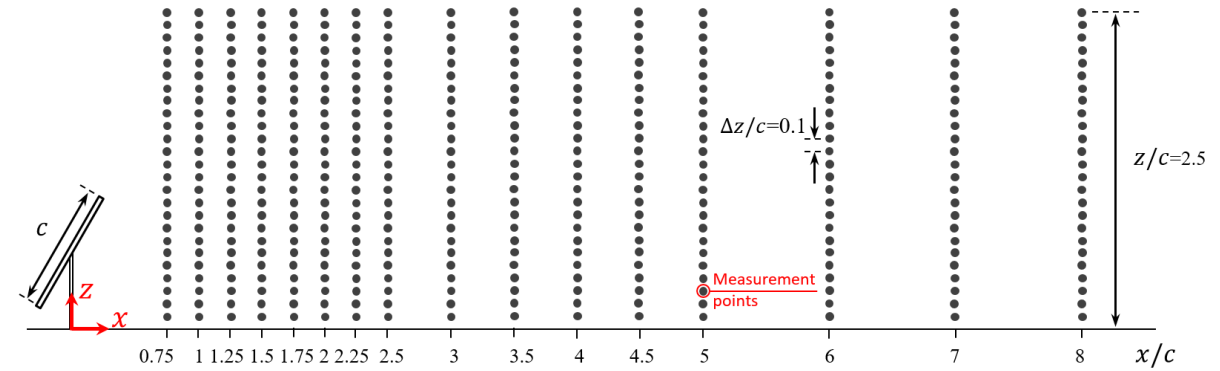
(approximately 1 m). It must be noted that larger errors may exist in the immediate proximity of the plate in the wake, at $x/c \leq 1$ where turbulence intensity is very large.



Figure 3: A schematic showing the locations of velocity measurements in the wake.

## 3    Wake Flow Characteristics

### 3.1    Velocity Deficit

Figure 4 shows the time-averaged streamwise velocity deficit in the $xz$-plane in the wake for the three elevation angles and the two inflow conditions. The velocity deficit normalised with the free-stream velocity, $(U_{in} - U)/U_\infty$, at the central line, $y=0$, is presented. A distinct region of velocity deficit exists in the wake of the plates up to $x/c=5$ for all three elevation angles, with the largest deficit observed when $\alpha =90°$. Due to proximity to the ground and velocity gradient in the inflow boundary layer, the wakes are asymmetric. The accelerated flow regions, represented by the negative values, are also seen above the plate, $z/c >1.5$, and further downstream at $x/c >6$. Furthermore, the comparison of the mean velocity at $x/c=8$ with the inflow conditions shows that the wake flow has not yet recovered.

Comparison of the flow for the two incoming conditions in Figure 4 shows a slightly faster recovery of the wake for the incoming flow with the larger turbulence intensity, which is due to the increased entrainment of fluid into the wake.
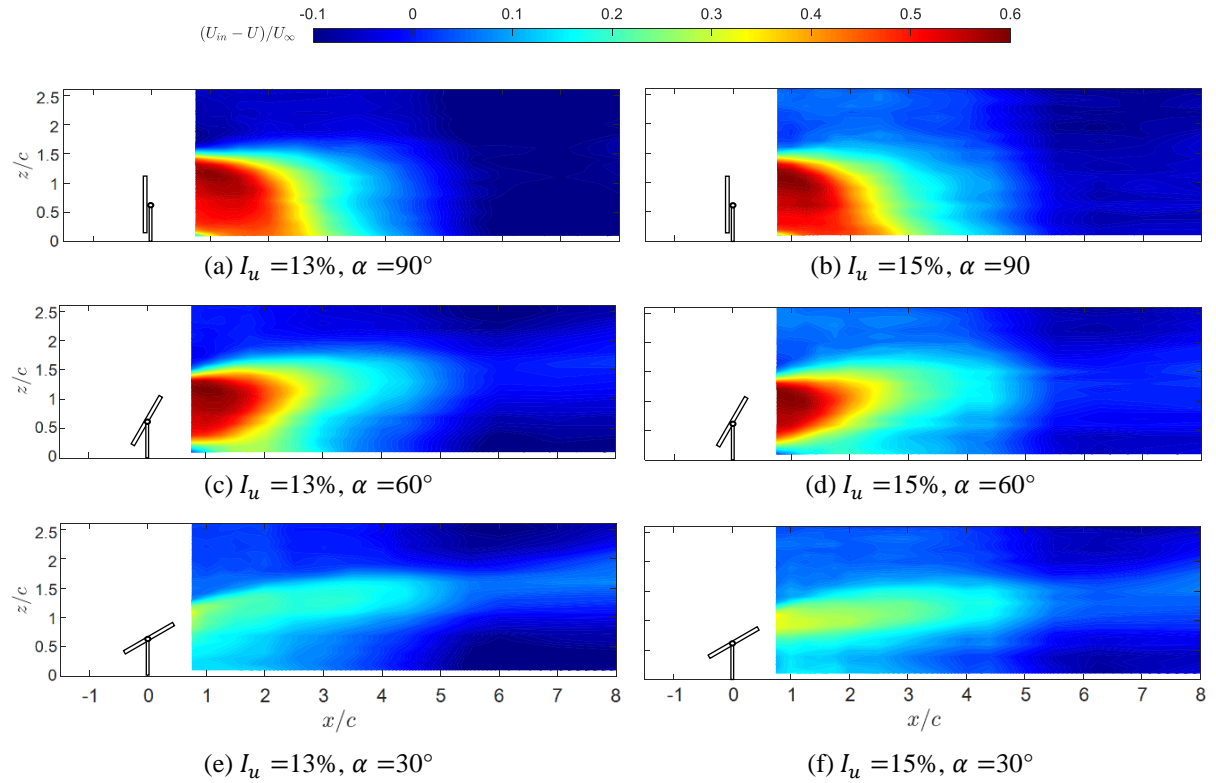
(a) $I_u =13\%$, $\alpha =90°$

(b) $I_u =15\%$, $\alpha =90$

(c) $I_u =13\%$, $\alpha =60°$

(d) $I_u =15\%$, $\alpha =60°$

(e) $I_u =13\%$, $\alpha =30°$

(f) $I_u =15\%$, $\alpha =30°$

Figure 4: Streamwise velocity deficit, $U_{in} - U$, normalised with freestream velocity, $U_\infty$, in the wake in the $xz$-plane for the two inflow boundary layers (left: Boundary Layer A, right: Boundary Layer B): (a–b) $\alpha =90°$, (c–d) $\alpha =60°$, (e–f) $\alpha =30°$.

Vertical profiles of the mean streamwise and vertical velocities at different streamwise distances are compared for the three elevation angles in Figure 5, where the streamwise velocity deficit and the wake-induced vertical velocity are clearly seen. In the near wake region, Figure 5(a), the variations of the streamwise and vertical velocities occur at different extents based on the elevation angle of the plate, for example at $x/c$=2 the reduction of streamwise velocity is the largest for $\alpha =90°$. The increased gap between the bottom edge of the plate and the ground at $\alpha =60°$ and $\alpha =30°$ creates a jet flow in this region which is more significant at $\alpha =30°$ resulting in a larger streamwise velocity compared to the other two angles and a positive vertical velocity. In the far wake, Figure 5(d), the differences diminish by $x/c$=8, and the profiles closely match one other, while still differ from the inflow profile in Figure 2(a).
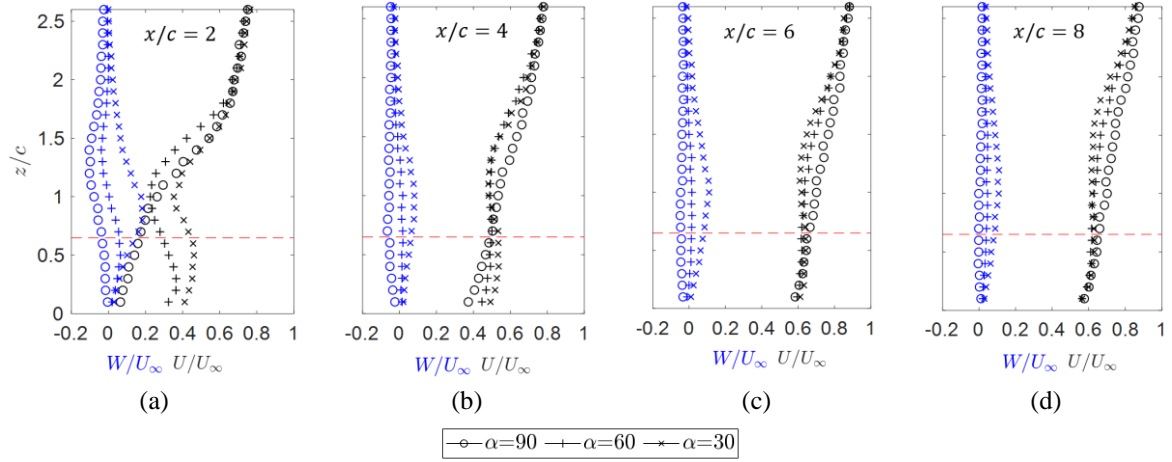
Figure 5: Vertical profiles of mean streamwise, $U$, and vertical velocity, $W$, at different streamwise locations in the wake in Boundary Layer B at $I_u$ =15% for $\alpha$ =90°, 60°, 30°: (a) $x/c$ =2, (b) $x/c$ =4, (c) $x/c$ =6, (d) $x/c$ =8. The black and blue colours represent the streamwise and vertical velocity, respectively. The horizontal dashed lines show the heliostat model hinge height.

### 3.2    Wake Turbulence

Figure 6 shows the normalised turbulence kinetic energy calculated from the variance of all three velocity components in the wake at different elevation angles and inflow conditions. As shown in Figure 6, there is a significant increase in turbulence kinetic energy in the near wake region, $x/c$ <4, which is caused by separation of flow at the edge of the plate. The increased turbulence kinetic energy region is mainly concentrated at the top edge of the plate and much less effect is seen at the bottom edge of the plate. This asymmetry is due to velocity gradient of the incoming boundary layer flow and the ground proximity where shear is smaller at lower heights.

Comparison of the turbulence kinetic energy for the plates at the three elevation angles shows that the increase in turbulence energy is larger for the plate at $\alpha$ =90° compared to $\alpha$ =60° and 30°. Furthermore, the regions of increased turbulence kinetic energy are extended further downstream for lower elevation angles which is due to the increased gap between the plate and the ground, forming a stronger wall jet in the gap region as discussed in (Krampa-Morlu and Balachandar, 2007; Shinneeb and Balachandar, 2016a).

The inflow condition has a slight impact on the turbulence kinetic energy distributions as shown in Figure 6. For instance, comparison of the turbulence kinetic energy at $\alpha$ =90° for the two inflow conditions, Figure 6(a) and Figure 6(b), shows a slightly larger peak of turbulence kinetic energy in the wake of the plate in boundary layer A. This can be attributed to the inflow conditions. The difference between the inflow turbulence intensities is not significant, ($I_u$ =13% and 15% in A and B, respectively). Hence, the larger shear, $\tau_H$, in

boundary layer A, which is twice that in boundary layer B, may be the source of the larger peak turbulence kinetic energy in the wake.
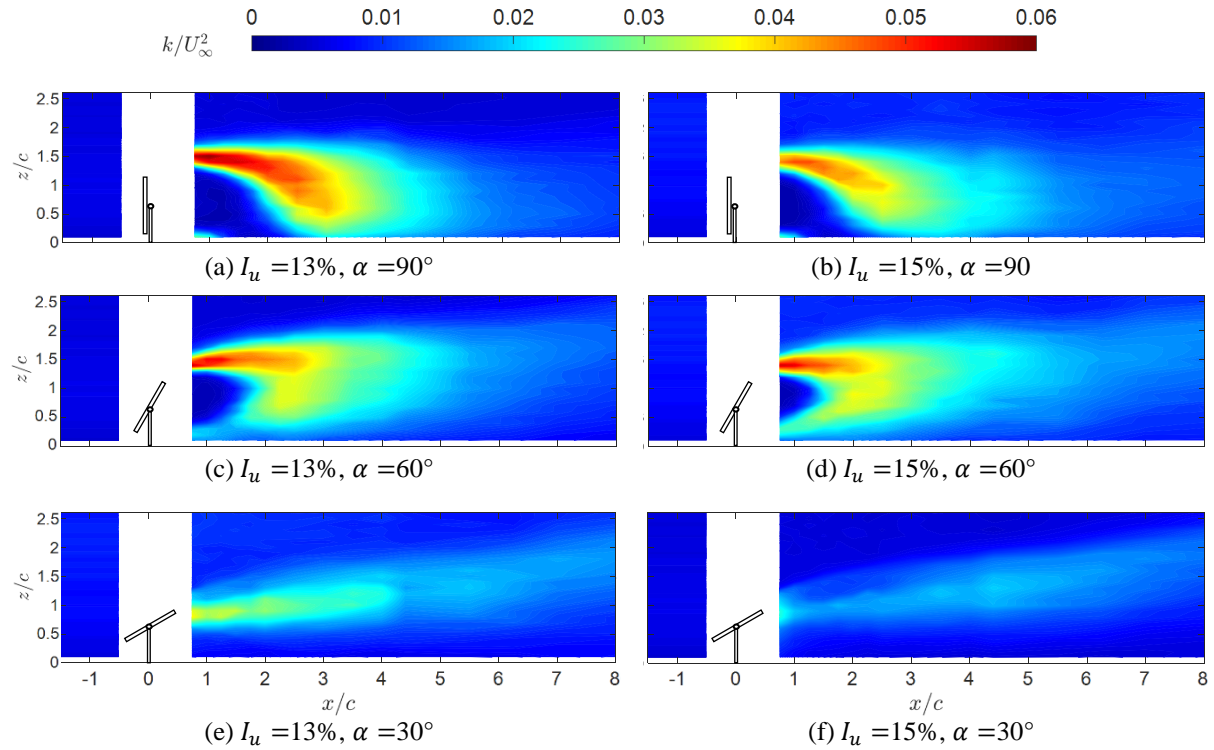


Figure 6: Normalised turbulence kinetic energy in the wake in the $xz$-plane for the two inflow boundary layers (left: Boundary Layer A, right: Boundary Layer B): (a–b) $\alpha$ =90°, (c–d) $\alpha$ =60°, (e–f) $\alpha$ =30°.

Figure 7 shows normalised Reynolds shear stress representing the vertical momentum flux for the different cases. Turbulent momentum fluxes indicate flow entrainment into the wake which significantly affects wake recovery. As shown in Figure 7, two regions of positive and negative Reynolds stress are seen for all cases. Large positive Reynolds stresses indicating downward momentum fluxes exist in the near wake at the top edge of the plate for $\alpha$ =90° and 60°, Figure 7(a–d), and upward momentum fluxes which are much smaller in magnitude exist at the bottom edge of the plate. Existence of the peak magnitudes at the top edge of the plate is due to the larger velocity gradient and shear at the top edge. At $\alpha$ =30°, Figure 7(e–f), due to the increased gap flow, the upward momentum fluxes are extended further downstream diminishing the extent and magnitude of the positive Reynolds stresses. Furthermore, the streamwise extent of the regions of positive and negative Reynolds stresses is larger for lower elevation angles, similar to the turbulence kinetic energy distributions.

Comparison of the shear stress distributions for the two inflow conditions shows that the regions of large Reynolds stress extend further downstream in boundary layer A. A similar effect is observed for the turbulence kinetic energy in Figure 6. The increased spatial extent of
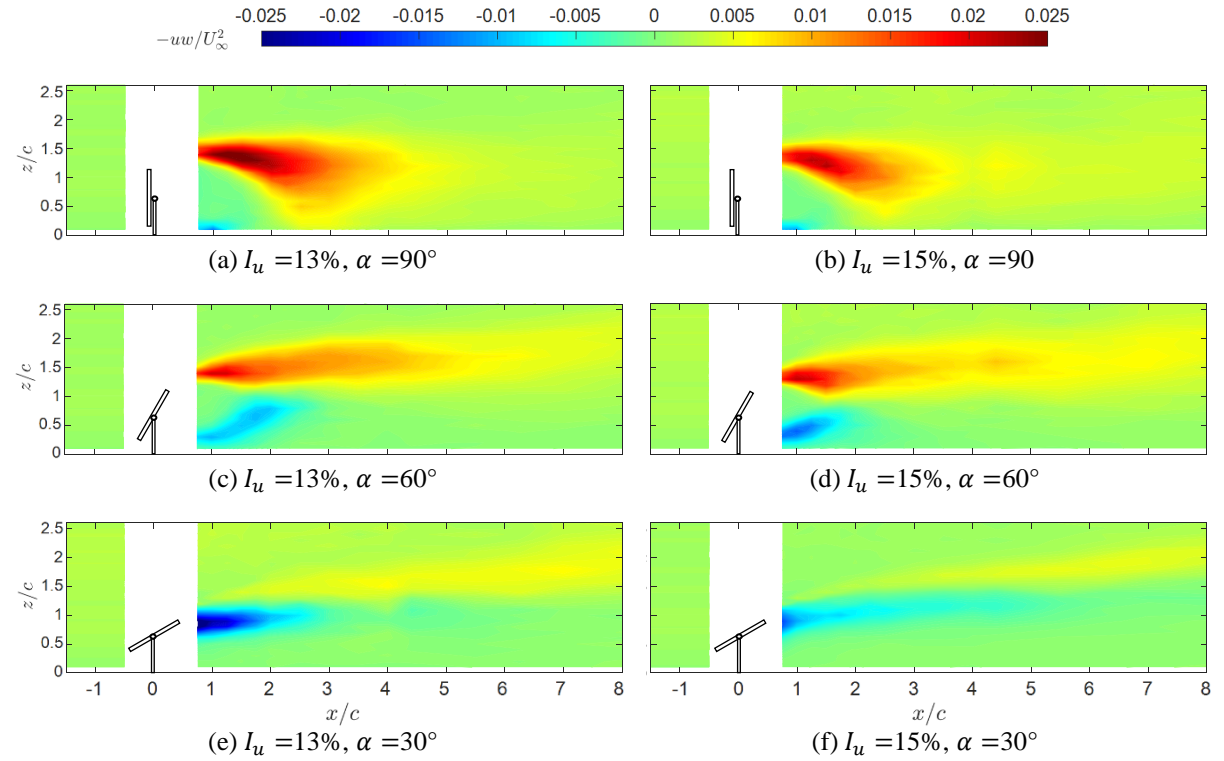
regions of large turbulence kinetic energy and Reynolds stress in boundary layer A is due to the larger mean shear and the lower turbulence intensity in boundary layer A (Table 1).



Figure 7: Normalised mean Reynolds shear stress in the wake in the $xz$-plane for the two inflow boundary layers (left: Boundary Layer A, right: Boundary Layer B): (a–b) $\alpha$ =90°, (c–d) $\alpha$ =60°, (e–f) $\alpha$ =30°.

### 3.3 Spectral Characteristics of Velocity Fluctuations

The power spectral density of the streamwise velocity fluctuations in the wake of the plate at $\alpha$ =90° is shown in Figure 8. The power spectral density pre-multiplied by frequency and normalised with the velocity variance, $fS_{uu}/\sigma_u^2$, is presented. This non-dimensional form is chosen as it displays the frequencies which are the major carriers of energy in the flow. As similar trends were found for the streamwise and vertical velocity spectra, only the results for the streamwise velocity are presented here. Figure 8(a) shows the normalised spectra in the near wake region, $x/c$=1, at different vertical heights inside and outside the wake flow. A clear distinction between the spectral distributions in the wake, $z/c$=0.5–1, and outside the wake, $z/c$=2–2.5, is found. Outside the wake flow, at $z/c$=2–2.5, the peak of the spectrum is at $fc/U_\infty$ =0.03, which is the dominant peak of the turbulent boundary layer flow corresponding to the integral length scale. There is an increase in the energy of non-dimensional frequencies $fc/U_\infty$ >0.1 at $z/c$=1.5, which is the location of increased turbulent kinetic energy (Figure 6(a)). When descending further into the wake flow, $z/c$=0.5–1, the spectral distribution changes drastically showing transfer of energy to high frequencies such that the inflow peak

diminishes. The transfer of energy from the large-scale turbulence structures to the small scales shows the breakdown of large inflow turbulence structures by the plate.

Figure 8(b) shows the power spectral density in the wake of the plate at $\alpha =90°$ and the plate hinge height, $z/c$=0.65, at several downstream distances. The turbulence spectrum of the incoming boundary layer is also shown. At $x/c$=1, the higher frequencies have the highest energy which shows the existence of smaller turbulence scales and breakdown of the larger inflow turbulence structures. At $x/c$=2, an increased energy level at the higher end of the spectrum is seen showing the remainder of the wake-induced small vortices. Further downstream, in the far wake region, $x/c$=4 to 8, the spectral distribution is more similar to the inflow although containing higher energy at the mid- to high frequencies, $fc/U_\infty$ >0.1, compared to the inflow. Furthermore, comparison of the spectrum at $x/c$=8 with the inflow spectrum shows that the wake flow has not fully recovered up to $x/c$=8 (as also shown in mean velocity contours in Figure 4).

The results in Figure 8 show no dominant shedding peak in the turbulence spectrum making it difficult to determine a unique Strouhal number for vortex shedding. Instead, an increase in the energy of a range of turbulence scales is identified. Lack of a distinguished shedding frequency in the wake was also found by Hearst *et al.* (2016) in the wake of a cube exposed to free-stream turbulence, where an increase in the energy over a range of frequencies was observed instead of a prominent shedding frequency. Rind and Castro (2012) also found that inflow turbulence damped vortex shedding and reduced its energy, such that at high inflow turbulence intensities the trace of vortex shedding in the turbulence spectrum was hardly visible.
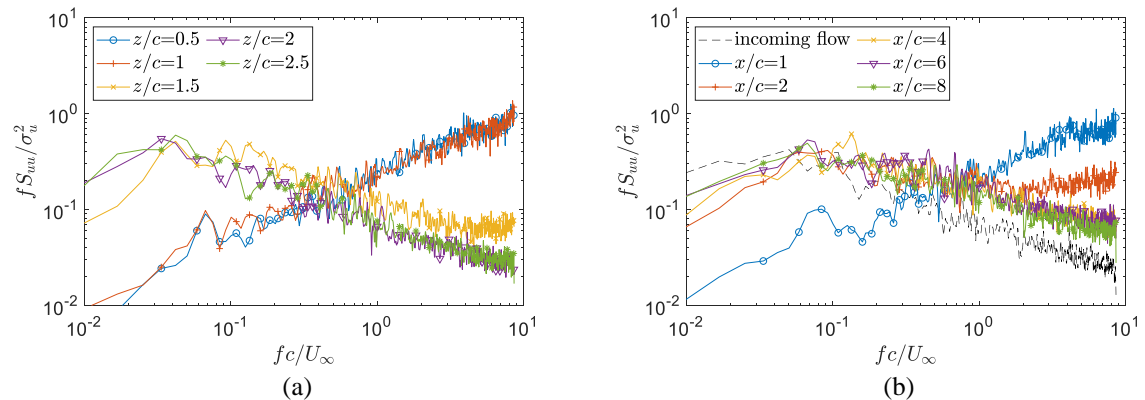


Figure 8: Normalised power spectral density of streamwise velocity fluctuations, $fS_{uu}/\sigma_u^2$, in the wake for $\alpha$=90°: (a) at several vertical positions at $x/c$=1, (b) at several downstream positions at $z/c$=0.65.

Figure 9 shows the normalised spectral density of streamwise velocity fluctuations at $z/c$=0.65 at several downstream distances for the plate at $\alpha$ =60° and $\alpha$ =30°. For both elevation angles, increase of higher-frequency turbulent scales is evident in both the near and far wake regions showing that the plate at both elevation angles breaks down the large inflow turbulence structures. To identify the effect of the elevation angle, the near wake spectra at the hinge height for the three elevation angles are compared in Figure 9(c–d), which show the energy transfer is more significant at $\alpha$ =90°.
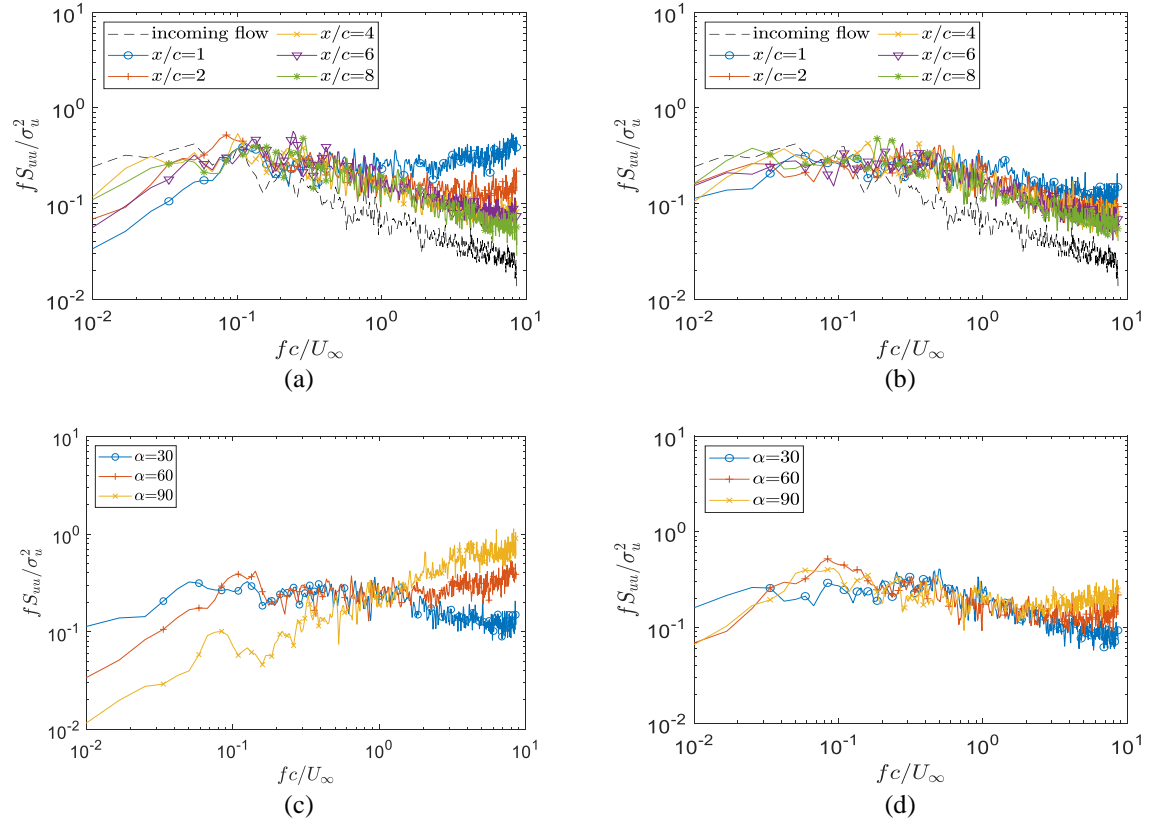


Figure 9: Normalised power spectral density of streamwise velocity fluctuations, $fS_{uu}/\sigma_u^2$, in the wake at $z/c$=0.65: (a–b) at several downstream locations for $\alpha$=60° and $\alpha$=30°, (c–d) comparison of the spectra for the three elevation angles at $x/c$=1 and $x/c$=2, respectively.

## 3.4    Orthogonal Wavelet Decomposition of Velocity Fluctuations

To determine the most energetic scales in the wake flow, the orthogonal wavelet method is employed in this study to decompose velocity according to the scales of turbulence structures. Using the wavelet multi-resolution technique, the velocity signal is broken down into frequency bands which directly represent the scales of turbulent structures (Razali *et al.*, 2010). The decomposed velocity signals corresponding to each level can then be analysed individually in time or frequency domain providing detailed information about each specific

turbulence scale. Using this method, a better understanding of the various scales in the wake flow can be achieved. This method has been used in the literature for analysis of turbulent structures in wake flows (Rinoshika and Zhou, 2005; Zhou *et al.*, 2006; Rinoshika and Zhou, 2007; Razali *et al.*, 2010; Rinoshika and Omori, 2011; Ali *et al.*, 2016). Further details of the orthogonal wavelet method are given in (Rinoshika and Zhou, 2005; Razali *et al.*, 2010).

The wavelet basis function used in this study is the Daubechies wavelet with an order of 20, as according to Rinoshika and Zhou (2007) the Daubechies is a suitable filter for turbulence analysis due to its smoothness and frequency localisation. Using the orthogonal discrete wavelet transform, the streamwise and vertical velocity signals are decomposed into 10 levels. The wavelet component of the velocity signal in each level provides information about the turbulent structures in its corresponding frequency band regardless of the number of wavelet levels. The frequency bands corresponding to each wavelet level are shown on the spectra of longitudinal and vertical velocity fluctuations in Figure 10. The higher wavelet levels correspond to lower frequencies and larger turbulence structures. The longitudinal and vertical integral length scales of turbulence are also shown in Figure 10. As shown in Figure 10, Levels 8–10 and Levels 7–10 represent the turbulent structures larger than the streamwise, $L_u^x$, and vertical, $L_w^x$, integral length scales.
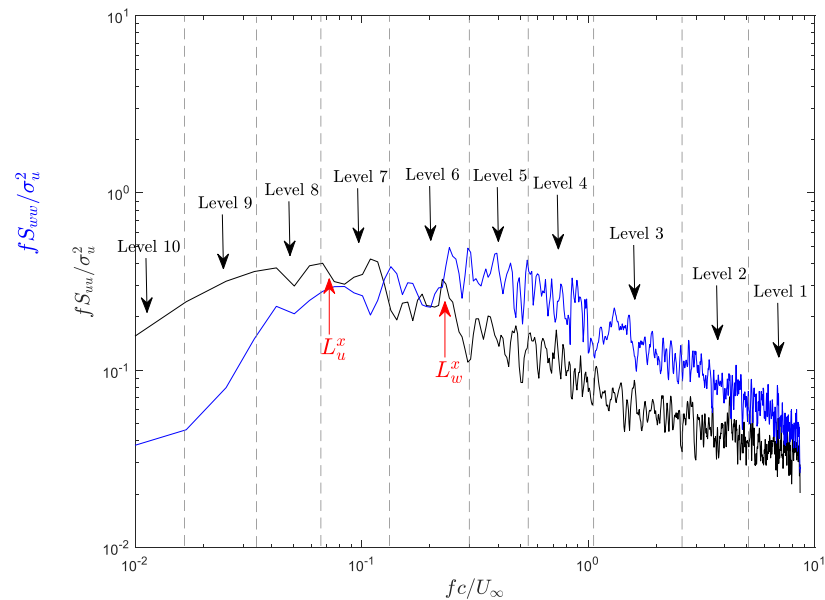


Figure 10: The normalised frequency bandwidth of the wavelet levels shown on the spectra of streamwise and vertical velocity fluctuations, the black and blue lines, respectively, in Boundary Layer B.

After decomposing the velocity signal into different scales, the variance of each scale is calculated. By comparison of the variance of each wavelet level to the variance of the original velocity signal, the contributions to velocity variance from different scales are found. Figures 11(a) and 11(c) show the normalised variance of streamwise and vertical velocity in the wake of the plate at $\alpha$=90° at $z/c$=0.65 from $x/c$=0.75 to $x/c$=8. The streamwise and vertical velocity variances in the wake increase to reach a peak at $x/c$=2.5 and 3, respectively, which is then followed by a decrease in the variance (the same trend as turbulent kinetic energy in Figure 6). The normalised variance of the wavelet levels of the streamwise and vertical velocity components in the wake is shown in Figure 11(b) and 11(d), respectively. According to Figure 11(b), the variances of wavelet Levels 1–3, which represent the small turbulence structures, remain almost constant along the streamwise direction. In contrast, the variances of large scales, wavelet Levels 8–10, increase significantly reaching a peak at $x/c$=2.5. According to Figure 11(b) and Figure 11(d), in the near wake region at $x/c$=1, the variances of all 10 levels are almost in the same order due to the breakdown of large scales to smaller scales which leads to reduction of energy of large scales, which agrees with the spectral analysis in Figure 8. Further downstream as the large scales grow, their energy increases and the variances of Levels 8–10 increase by four to five times between $x/c$=2 and $x/c$=8. A similar trend is observed in Figure 11(d) for the variances of the wavelet components of vertical velocity showing that the large turbulence structures are the major contributors to the peak of the vertical velocity variance, which occurs at $x/c$=3 and further downstream, while at $x/c$=1 the breakdown of large scales to smaller scales results in a significant reduction in the variance of large scales. These results along with the spectral analysis show that the dominant mechanism in close proximity of the plate in the near wake is breakdown of large-scale turbulence structures of the inflow boundary layer and transfer of energy to small scales. When moving further downstream, the flow starts to recover, and turbulence scales develop towards the inflow distribution. Evolution of turbulence structures towards the external turbulence was also found in the in the far wake of a sphere exposed to inflow turbulence by Rind and Castro (2012).
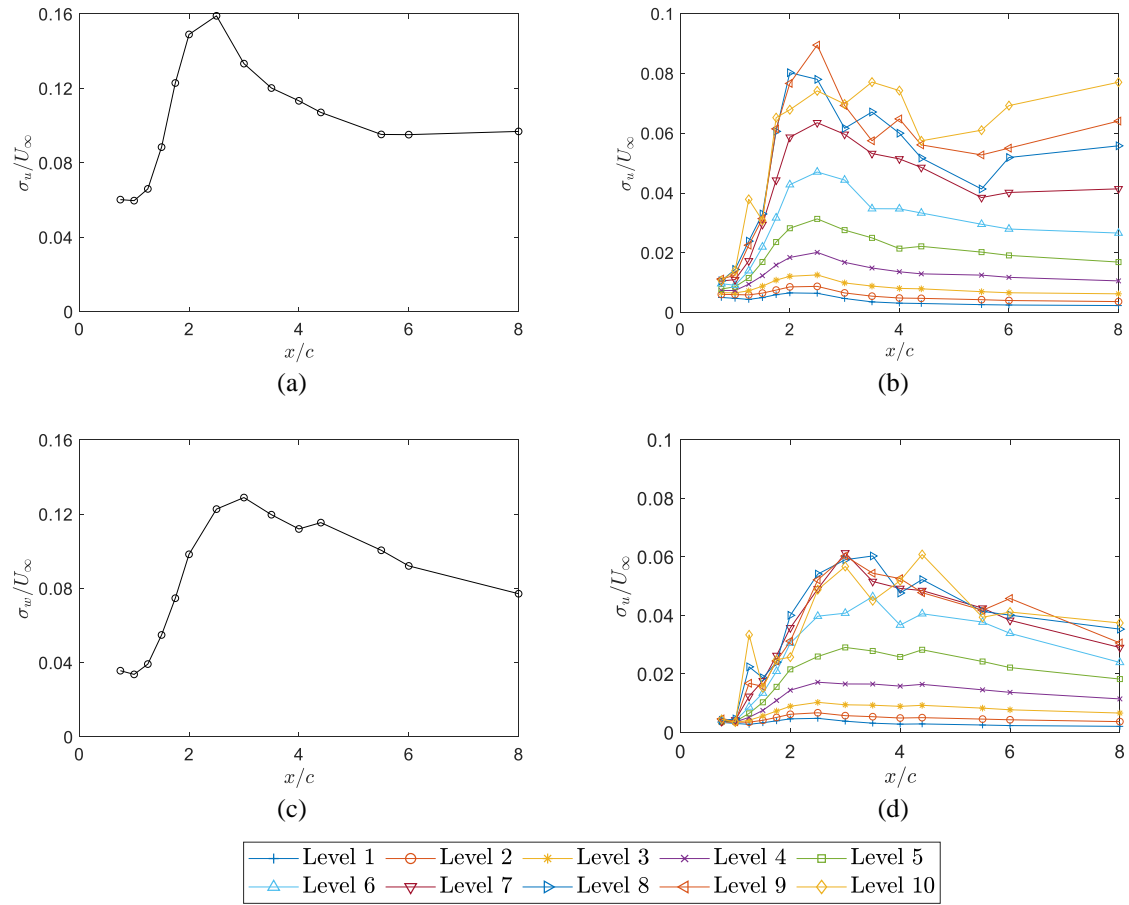
Figure 11: Normalised velocity variance in the wake in streamwise direction for $\alpha$=90° at $z/c$= 0.65: (a–b) variance of streamwise velocity and its wavelet levels, (c–d) variance of vertical velocity and its wavelet levels.

Figure 12 shows the normalised variance of the wavelet levels of the streamwise velocity component in the wake at $z/c$=0.65 for $\alpha$ =60° and $\alpha$ =30°. The streamwise distribution of the different wavelet levels in Figure 12(a) for $\alpha$ =60° is similar to that in Figure 11(b) for $\alpha$ =90° with a slightly larger magnitude of the variance of the large scales in the proximity of the plate. For $\alpha$ =30°, Figure 12(b), no significant change in the streamwise distribution of the variances of the different levels is observed indicating that there is much less breakdown of large scales by the plate compared to the other two elevation angles. This agrees with the results found from the spectral distributions in Figure 9(b).
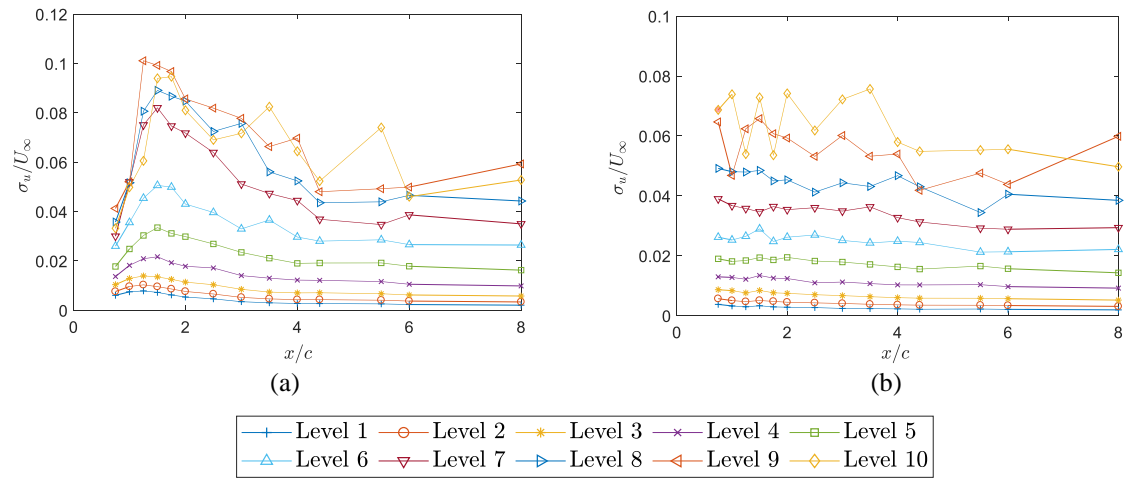
Figure 12: Normalised variance of the wavelet levels of streamwise velocity component in streamwise direction at $z/c= 0.65$ in the wake for: (a) $\alpha=60°$, (b) $\alpha=30°$.

The wavelet analysis results show a transfer of energy to smaller turbulence scales in the immediate downstream of the heliostat, while at $x/c >2$, the large turbulence scales in the order of the integral length scale of the inflow boundary layer have larger turbulence intensities. Since the length scales of turbulence and their corresponding intensity can directly impact the wind loads on structures placed in the wake flow, these results can have important implications for the dynamic wind loads in an array of heliostats, which are discussed in Section 4.

## 4   Wake-induced wind loads in a heliostat field

The results in Section 3 provide an insight into the velocity and turbulence characteristics in the wake of a model heliostat in a simulated atmospheric boundary layer flow. In a heliostat field, the heliostats which are placed inside the field are exposed to the wake flow of the upstream heliostats. Although the presence of the other heliostats in the wake affects the flow, the wake characteristics can be used as a basis for prediction of the flow characteristics in the field. As the flow turbulence characteristics are directly related to the wind loads on heliostats, the findings in Section 3 can have several implications for the design of heliostat fields which are discussed in this section.

A summary of changes in mean velocity and velocity variances in the wake flow compared to the inflow boundary layer is presented in Figure 13. To highlight how the flow in the wake changes from the inflow atmospheric boundary layer, the mean velocity, streamwise and vertical velocity variances, and the streamwise and vertical turbulence intensities in the wake are normalised with their inflow values and are given for the plates at the three elevation angles. According to Figure 13, despite the decrease in mean wake velocity, the velocity

variance is larger than the inflow condition. Except at $x/c <1.5$ for $\alpha=90°$, both the streamwise and vertical velocity variances are larger in the wake for all other cases. The increase of velocity variance accompanied with the reduction of mean velocity leads to an increased turbulence intensity, such that both the streamwise and vertical turbulence intensities are larger than the inflow at $x/c <5$ for all the three elevation angles. The maximum velocity variances in the wake flow for all three elevation angles occur at approximately $x/c =2$, where the velocity variance is more than double the inflow value. The maximum turbulence intensity at the heliostat hinge height occurs at $x/c =1.5$ with more than 12-times increase in turbulence intensity for $\alpha=90°$ and $60°$, Figure 12(a–b).
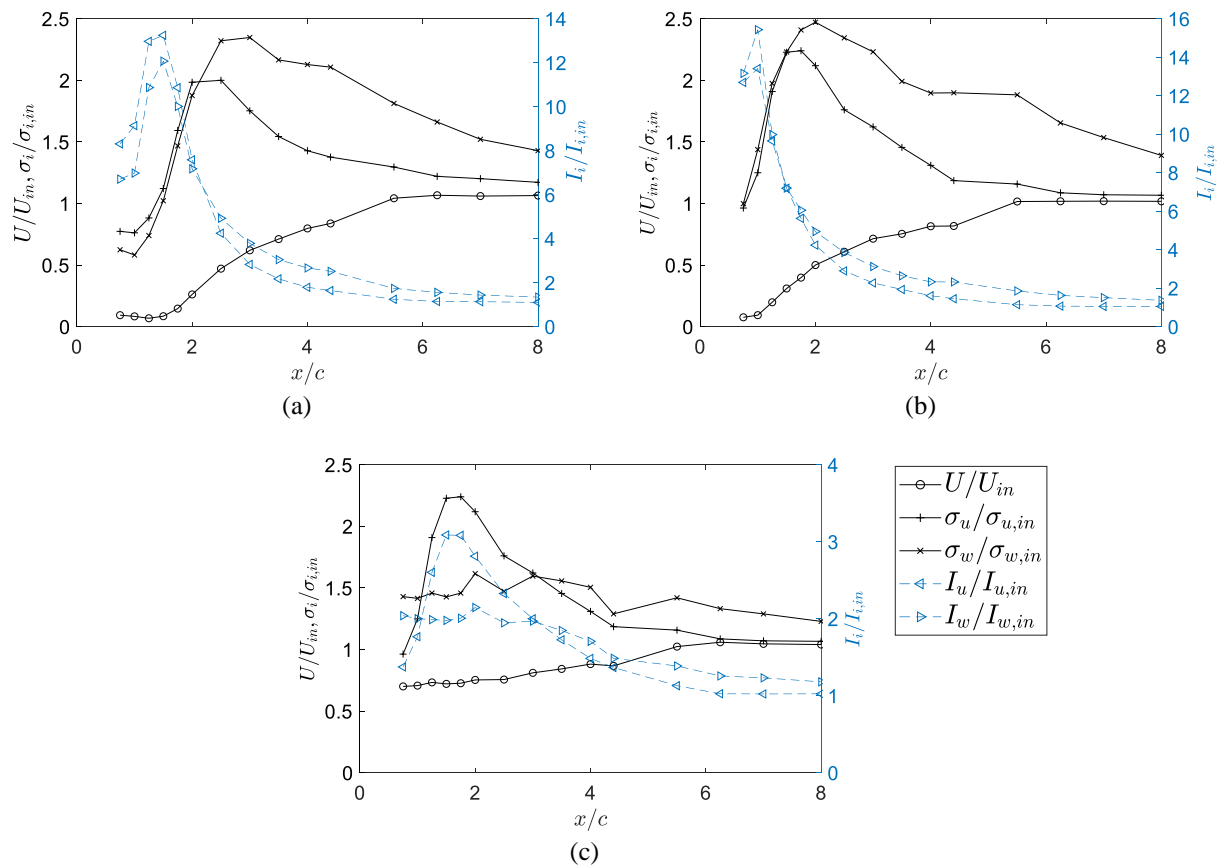


Figure 13: The changes in velocity and turbulence in the wake compared to their inflow values, represented by the subscript *'in'*, at the plate hinge height, $z/c$=0.65, for (a) $\alpha$=90°, (b) $\alpha$=60°, and (c) $\alpha$=30°. In each figure, the black solid lines show magnitude of normalised mean velocity, streamwise and vertical velocity variances on the left axis and the blue dashed lines show the normalised streamwise and vertical turbulence intensities on the right axis.

## 4.1   Operating wind loads

Figure 13 shows that velocity variance and turbulence intensity in the wake are in general larger than the inflow boundary layer. Hence, the heliostats positioned inside the field are exposed to an increased turbulence intensity compared to the heliostats in the first row, which

is in agreement with the field measurements by Sment and Ho (2014). Since the increased turbulence intensity is directly correlated with an increase in unsteady forces (Bearman, 1971; Peterka *et al.*, 1989; Jafari *et al.*, 2018; Pfahl, 2018), the unsteady wind loads on the in-field heliostats are expected to be larger than the wind loads on the heliostats in the first row. For instance, according to Figure 13(a), $I_u$ in the wake of a heliostat at $\alpha$=90° at $x/c$ =2 increases to a value 7-times larger than the inflow turbulence intensity. If a second heliostat is placed at this location, it will be exposed to $I_u = 7.6\ I_{u,in}$. Such increase in turbulence intensity will lead to more than 80% increase in the unsteady drag force coefficient on the second heliostat according to the relationship given in Jafari *et al.* (2018). Hence, a significant increase in the unsteady loads on the downstream heliostats in a field is expected due to the increase of turbulence intensity.

The changes in wind loads predicted from the wake turbulence is confirmed by experimental measurements of wind loads on tandem heliostats. Measurements of pressure distribution on two heliostat models placed in tandem show that the pressure distribution on the heliostat panel varies significantly as the gap between the two heliostats changes leading to variations in the position of the centre of pressure (Jafari *et al.*, 2019a), which can be attributed to the turbulence in the wake of the upstream heliostat. The standard deviation of the position of centre of pressure, representing the unsteady variations of the pressure distribution on the downstream heliostat panel, was found to be larger than the single heliostat when the gap between the two heliostats, $x/c$, varied between 1 and 7 reaching a peak at $x/c$=2 (Jafari *et al.*, 2019a). Furthermore, the standard deviation of the position of centre of pressure was the largest when both plates were elevated at 90° which shows the effect of the dramatically increased turbulence intensity in the wake of the heliostat at $\alpha$=90°.

As the magnitude of the forces on the panel and the position of the centre of pressure vary, the induced moments at the heliostat hinge and pylon base change, which is important for the design of elevation drives and foundation. Figure 14 shows the hinge moment coefficient, $C_{MHy}$, on the second tandem heliostat compared to the single heliostat based on the experimental measurements by (Jafari *et al.*, 2019a). The mean and peak coefficients and the root mean square (RMS) of the fluctuating coefficient normalised with those on a single heliostat are shown. It is observed that the peak and RMS coefficients are larger than those for the single heliostat for all the gap ratios for $\alpha$=90° and 60°, and at $x/c \geq 2$ for $\alpha$=30°. The increase in the peak and RMS coefficients is larger for $\alpha$=90° and 60° compared to $\alpha$=30° which shows the effect of the larger increase in turbulence intensity in the wake of the heliostat

at the two larger elevation angles. Moreover, the results of Figure 14 show an increase in the mean hinge moment coefficient at $x/c \geq 2$ for $\alpha=30°$ and $60°$ and $x/c=3$–4 for $\alpha=90°$. The increase of mean hinge moment is despite the reduction of mean lift and drag force coefficients reported by Peterka *et al.* (1987a) for the heliostats in five downstream rows, which is due to the reduction of mean velocity in the wake of the upstream heliostat. Larger mean hinge moment coefficient, in spite of lower mean lift and drag force coefficients, is attributed to the unsteady variations of the position of the centre of pressure as reported by Jafari *et al.* (2019a), and is a consequence of the increase of turbulence intensity and variation of the length scales of turbulence in the wake of the upstream heliostat. Hence, the increase in turbulence intensity in the wake of a heliostat not only leads to an increase in the fluctuating lift and drag forces on the downstream heliostat, but may also lead to an increase of the mean hinge moment coefficient. This highlights the importance of modification of heliostat design for the heliostats positioned inside the field compared to those at the front rows.
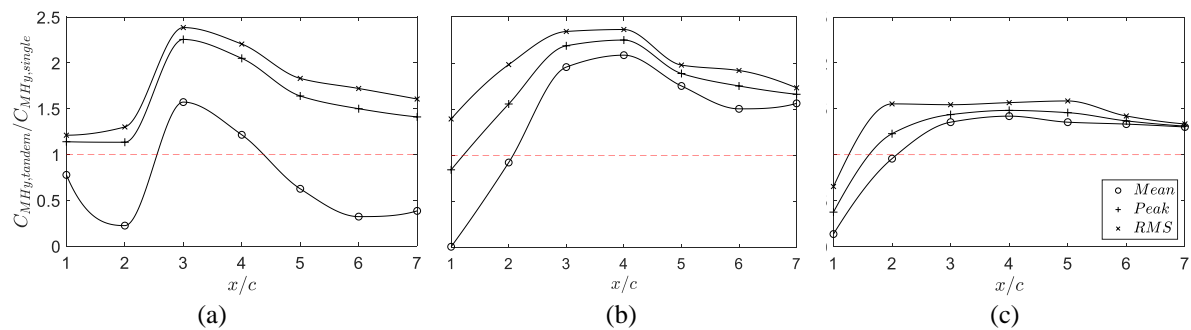


Figure 14: The mean, peak and RMS hinge moment coefficient, $C_{MHy}$, on a second tandem heliostat normalised against the moment coefficients on a single heliostat for (a) $\alpha=90°$, (b) $\alpha=60°$, and (c) $\alpha=30°$. Reproduced from Jafari *et al.* (2019a).

### 4.2   Effect of field density on operating wind loads

Since the wake flow characteristics are found to vary at different streamwise distances, the distance between the rows in a heliostat field, which is indicated by field density, is an important parameter affecting the flow and the wind loads. According to Figure 13, the maximum turbulence intensity in the wake flow for all three elevation angles occurs at approximately $x/c = 1.5$, and both streamwise and vertical turbulence intensities are significantly larger at $x/c \leq 3$ being more than 4-times larger than the inflow for $\alpha=90°$ and $60°$ and double the inflow for $\alpha=30°$ (Figure 13). Hence, in high density areas of a heliostat field, where the gap between the heliostat rows is between 1–3 times the characteristic length, the unsteady wind loads are expected to be larger than other regions of the field indicating a

critical design case. The increase in the unsteady wind loads on the inner field heliostats is expected to be less in regions of the field with a very low density, $x/c > 6$, as the increase in the turbulence intensity is less than 20%, where the 20% increase is for $\alpha = 90°$. Hence, the wind loads on heliostats in the low-density regions near the perimeter of the field are likely to show a smaller variation with distance into the field than those in high-density regions close to the tower. The predicted effects are in agreement with the pressure measurements on tandem heliostats which show the largest variations of the position of the centre of pressure at $x/c = 1$–3 (Jafari *et al.*, 2019a) and the maximum hinge moment coefficients at $x/c = 3$ for $\alpha = 90°$ and 60° (Figure 14).

Field density can also affect the dominant frequencies and scales of turbulence in the flow. Based on the spectral analysis of wake turbulence, it was found that the spectral distribution of turbulence in the immediate wake at $x/c = 1$ differs significantly from the atmospheric boundary layer spectrum showing an increase of small scale turbulence structures and breakdown of the larger inflow turbulence structures (Figure 8). The wavelet analysis also showed that the different frequency bands of turbulence spectrum have a similar variance, without a prominent peak at the heliostat hinge height at $x/c = 1$ (Figure 11). In contrast for $x/c > 2$, the frequencies with the peak variance and energy are the same as the peak frequencies of the inflow boundary layer. The peak frequencies in the wake flow at $x/c > 2$ are therefore dominated by the incoming flow. As the minimum gap ratio in a heliostat field is typically larger than $x/c = 1$ (Hui, 2011), for gaps between the rows in a dense region of a field where $x/c \leq 2$, the spectral content of the flow will differ significantly from the inflow boundary layer. In contrast, peak frequencies of the velocity fluctuations in the field in regions where $x/c > 2$ will be similar to the atmospheric boundary layer flow. As the unsteady wind loads and the length scales of turbulence in the flow are strongly correlated (Jafari *et al.*, 2019c), these changes will affect the unsteady wind loads on heliostats in very dense regions. Furthermore, Emes *et al.* (2018) found that the frequency of peak pressure fluctuations at the leading edge of a heliostat at $\alpha = 0°$ matches the frequency corresponding to the integral length scale of the flow. Hence, the variation of the spectral distribution of turbulence in the wake may change the dominant frequency of the fluctuating forces on downstream heliostats in high density regions. This indicates the necessity for further investigation of dynamic wind loads for the heliostat field in future due to the possible implications it may have such as dynamic coupling of the unsteady forces and the natural frequency of the heliostat structure.

### 4.3 Stow wind loads

During periods of high wind speeds, heliostats are usually stowed by aligning the mirror panel horizontally to reduce the mean wind loads. The unsteady forces on the stowed heliostats in the turbulent atmospheric flow however can be large due to the large vertical velocity variance which is correlated with the unsteady lift force on stowed heliostats (Jafari *et al.*, 2019b). The peak turbulence-induced forces are critical for survivability of the heliostat structure since heliostats need to withstand the largest wind speeds at stow position. Partial stowing of a heliostat field has been suggested to increase the field operation hours over a larger range of wind speeds such that heliostats in regions of predicted larger wind load coefficients are stowed at lower mean wind speeds, with other regions of the field still in operation (Pfahl *et al.*, 2017). Such stowing strategies require a reliable estimation of the wind loads in different regions of the field in order to determine the regions which need to go to stow. Based on the wind direction, the stowed heliostats may be positioned in the wake of the heliostats which are still in operation. As according to Figure 13, the vertical velocity variance and turbulence intensity in the wake of the operating heliostats for all three elevation angles are always larger than the inflow, the stowed heliostats will be exposed to increased vertical turbulence intensity. For instance, vertical turbulence intensity in the wake of a heliostat at $\alpha = 30°$ at $x/c = 2$ is approximately double its inflow level according to Figure 13(c). If a stowed heliostat is placed in the wake of the mentioned heliostat at $x/c = 2$, the doubled vertical velocity will subject it to 40% increase in the peak lift force coefficient according to Jafari *et al.* (2019b). Hence, the results of this study show that in addition to mean wind speed as the criteria for partial stowing, vertical turbulence intensity in the field must also be considered.

## 5 Conclusions

The mean and spectral turbulence characteristics in the wake of a flat plate placed in turbulent atmospheric boundary layers were investigated. The results showed a significant increase in turbulence kinetic energy in the near wake region, $x/c < 4$ at the top edge of the plate. The increase in turbulence kinetic energy was the largest for $\alpha = 90°$ and the lowest for $\alpha = 30°$. Spectral analysis of velocity fluctuations in the wake showed two distinct regions. There was an increase in high frequencies and smaller scales of turbulence structures at $x/c \leq 2$, while in the far wake region, $x/c = 4–8$, the spectral distribution was a closer match to the incoming turbulent boundary layer. Furthermore, the variances of the streamwise and vertical velocity components were compared to the variances of their wavelet levels. It was found that in the immediate wake region, $x/c = 1$, breakdown of large inflow turbulence structures to

smaller scales was the dominant effect. When moving further downstream turbulence within the wake evolved towards the external turbulence structure.

The results of this study were applied to predict the wake-induced turbulence in a heliostat field. It is acknowledged that the presence of the downstream heliostats in the wake affects the flow pattern and the flow around multiple heliostats is more complex compared to a single heliostat. The results of the wake of a single heliostat could however be used as a basis for estimation of the turbulence changes in a heliostat field and consequently the wind loads. Based on this analysis, it was proposed that due to the increased turbulence intensity in the wake flow, the unsteady wind loads on the in-field heliostats increased compared to the front row, with a peak at high density areas of a field where the gap between the heliostat rows is between one to three times the characteristic length of the heliostat panel. Depending on the wind direction, the high-density regions of a field, which are typically positioned close to the tower, may be positioned in the wake of their upstream heliostats. Although the mean wind speed is lower in the wake, they are subjected to higher turbulence intensities in the wake of the upstream heliostats, which highlights the importance of dynamic wind loading for design of heliostats in regions of high density. Further studies in future are required to investigate the dynamic wind loading in different regions of a field, and to determine the effect of the field layout and wind direction on the wake flow.

## Acknowledgements

## Data Availability Statement

The data that supports the findings of this study are available within the article.

# References

Ali, N., Kadum, H. F., and Cal, R. B. 2016. Focused-based multifractal analysis of the wake in a wind turbine array utilizing proper orthogonal decomposition, *Journal of Renewable and Sustainable Energy*, 8: 063306.

Aliferis, A. D., Jessen, M. S., Bracchi, T., and Hearst, R. J. 2019. Performance and wake of a Savonius vertical-axis wind turbine under different incoming conditions, *Wind Energy*: 1-14.

Amoura, Z., Roig, V., Risso, F., and Billet, A.-M. 2010. Attenuation of the wake of a sphere in an intense incident turbulence with large length scales, *Physics of Fluids*, 22: 055105.

Barlow, J. B., Rae, W. H., and Pope, A. 1999. *Low-Speed Wind Tunnel Testing*, Wiley.

Bearman, P. W. 1971. An investigation of the forces on flat plates normal to a turbulent flow, *Journal of Fluid Mechanics*, 46: 177-98.

Bearman, P. W., and Zdravkovich, M. M. 1978. Flow around a circular cylinder near a plane boundary, *Journal of Fluid Mechanics*, 89: 33-47.

Bell, J. R., Burton, D., Thompson, M., Herbst, A., and Sheridan, J. 2014. Wind tunnel analysis of the slipstream and wake of a high-speed train, *Journal of Wind Engineering and Industrial Aerodynamics*, 134: 122-38.

Boddupalli, N., Yadav, N. K., and Chandra, L. 2018. The unsteady flow features behind a heliostat in a narrow channel at a high Reynolds number: Experiment and Large Eddy Simulation, *International Journal of Mechanical Sciences*, 136: 424-38.

Bosch, G., Kappler, M., and Rodi, W. 1996. Experiments on the flow past a square cylinder placed near a wall, *Experimental Thermal and Fluid Science*, 13: 292-305.

Draskovic, N. 2017. *Measurement methods in turbulent flows*, Master's Thesis, Norwegian University of Science and Technology.

Emes, M. J., Ghanadi, F., Arjomandi, M., and Kelso, R. M. 2018. Investigation of peak wind loads on tandem heliostats in stow position, *Renewable Energy*, 121: 548-58.

Gilhome, B. 2017. *Unsteady and time-averaged near-wake flow over the rear of sedan automobiles*, Doctorate, Doctorate Thesis, Monash University.

Hearst, R. J., Gomit, G., and Ganapathisubramani, B. 2016. Effect of turbulence on the wake of a wall-mounted cube, *Journal of Fluid Mechanics*, 804: 513-30.

Hui, T. M. 2011. *Design and optimization of heliostatt field using spinning-elevation sun tracking method based on computational analysis*, Master of Engineering Thesis, Universiti Tunku Abdul Rahman.

Humphries, W., and Vincent, J. H. 1976. Experiments to investigate transport processes in the near wakes of disks in turbulent air flow, *Journal of Fluid Mechanics*, 75: 737-49.

Jafari, A., Emes, M. J., Cazzolato, B. S., Ghanadi, F., and Arjomandi, M. 2019a. An Experimental investigation of unsteady pressure distribution on tandem heliostats. In *SolarPaces*. Daegu, AIP Conference Proceedings.

Jafari, A., Ghanadi, F., Arjomandi, M., Emes, M. J., and Cazzolato, B. S. 2019b. Correlating turbulence intensity and length scale with the unsteady lift force on flat plates in an atmospheric boundary layer flow, *Journal of Wind Engineering and Industrial Aerodynamics*, 189: 218-30.

Jafari, A., Ghanadi, F., Emes, M. J., Arjomandi, M., and Cazzolato, B. S. 2018. Effect of free-stream turbulence on the drag force on a flat plate. In *21st Australasian Fluid Mechanics Conference*. Adelaide, Australia.

Jafari, A., Ghanadi, F., Emes, M. J., Arjomandi, M., and Cazzolato, B. S. 2019c. Measurement of unsteady wind loads in a wind tunnel: Scaling of turbulence spectra, *Journal of Wind Engineering and Industrial Aerodynamics*, 193: 103955.

Kolb, G. J., Ho, C.K., Mancini, T.R., and Gary, J.A. 2011. Power tower technology roadmap and cost reduction plan, *SAND2011-2419, Sandia National Laboratories*.

Krampa-Morlu, F. N., and Balachandar, R. 2007. Flow recovery in the wake of a suspended flat plate, *Journal of Hydraulic Research*, 45: 270-78.

Lam, H. F., and Peng, H. Y. 2017. Measurements of the wake characteristics of co- and counter-rotating twin H-rotor vertical axis wind turbines, *Energy*, 131: 13-26.

Lam, K. M., and Leung, M. Y. H. 2005. Asymmetric vortex shedding flow past an inclined flat plate at high incidence, *European Journal of Mechanics - B/Fluids*, 24: 33-48.

Legendre, D., Merle, A., and Magnaudet, J. 2006. Wake of a spherical bubble or a solid sphere set fixed in a turbulent environment, *Physics of Fluids*, 18: 048102.

Nedić, J., Ganapathisubramani, B., and Vassilicos, J. C. 2013. Drag and near wake characteristics of flat plates normal to the flow with fractal edge geometries, *Fluid Dynamics Research*, 45: 061406.

Peng, H. Y., Lam, H. F., and Lee, C. F. 2016. Investigation into the wake aerodynamics of a five-straight-bladed vertical axis wind turbine by wind tunnel tests, *Journal of Wind Engineering and Industrial Aerodynamics*, 155: 23-35.

Peterka, J. A., Bienkiewicz, B., Hosoya, N., and Cermak, J. E. 1987a. Heliostat mean wind load reduction, *Energy*, 12: 261-67.

Peterka, J. A., Tan, L., Bienkiewcz, B., and Cermak, J. E. 1987b. Mean and peak wind load reduction on heliostats, *Technical Report for Colorado State University*.

Peterka, J. A., Tan, Z., Cermak, J. E., and Bienkiewicz, B. 1989. Mean and peak wind loads on heliostats, *Journal of Solar Energy Engineering*, 111: 158-64.

Pfahl, A. 2018. *Wind loads on heliostats and photovoltaic trackers*, Doctorate Thesis, Technische Universiteit Eindhoven.

Pfahl, A., Coventry, J., Röger, M., Wolfertstetter, F., Vásquez-Arango, J. F., Gross, F., Arjomandi, M., Schwarzbözl, P., Geiger, M., and Liedke, P. 2017. Progress in heliostat development, *Solar Energy*, 152: 3-37.

Razali, S. F. M., Zhou, T., Rinoshika, A., and Cheng, L. 2010. Wavelet analysis of the turbulent wake generated by an inclined circular cylinder, *Journal of Turbulence*, 11: N15.

Richards, P. J., Hoxey, R. P., Connell, B. D., and Lander, D. P. 2007. Wind-tunnel modelling of the Silsoe Cube, *Journal of Wind Engineering and Industrial Aerodynamics*, 95: 1384-99.

Rind, E., and Castro, I. P. 2012. On the effects of free-stream turbulence on axisymmetric disc wakes, *Experiments in Fluids*, 53: 301-18.

Rinoshika, A., and Omori, H. 2011. Orthogonal wavelet analysis of turbulent wakes behind various bluff bodies, *Experimental Thermal and Fluid Science*, 35: 1231-38.

Rinoshika, A., and Zhou, Y. 2007. Effects of initial conditions on wavelet-decomposed structures in a turbulent far-wake, *International Journal of Heat and Fluid Flow*, 28: 948-62.

Rinoshika, A., and Zhou, Y. U. 2005. Orthogonal wavelet multi-resolution analysis of a turbulent cylinder wake, *Journal of Fluid Mechanics*, 524: 229-48.

Shinneeb, A. M., and Balachandar, R. 2016a. Effect of gap flow on the shallow wake of a sharp-edged bluff body – mean velocity fields, *Journal of Turbulence*, 17: 94-121.

Shinneeb, A. M., and Balachandar, R. 2016b. Effect of gap flow on the shallow wake of a sharp-edged bluff body – turbulence parameters, *Journal of Turbulence*, 17: 122-55.

Sment, J., and Ho, C. K. 2014. Wind patterns over a heliostat field, *Energy Procedia*, 49: 229-38.

Tieleman, H. W. 2003. Wind tunnel simulation of wind loading on low-rise structures: A review, *Journal of Wind Engineering and Industrial Aerodynamics*, 91: 1627-49.

Vino, G., Watkins, S., and Mousley, P. 2003. The passenger vehicle wake under the influence of upstream turbulence. In., SAE Technical Paper 2003-01-0650.

Yang, D., Pettersen, B., Andersson, H. I., and Narasimhamurthy, V. D. 2012. Vortex shedding in flow past an inclined flat plate at high incidence, *Physics of Fluids*, 24: 084103.

Zhou, T., Rinoshika, A., Hao, Z., Zhou, Y., and Chua, L. P. 2006. Wavelet multiresolution analysis of the three vorticity components in a turbulent far wake, *Physical Review E*, 73: 036307.